Results in Engineering 22 (2024) 102205

Contents lists available at ScienceDirect

Results in Engineering

journal homepage: www.sciencedirect.com/journal/results-in-engineering

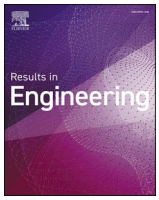

Fluid-thermal characteristics of solar-exhaust gas powered dryer: An experimental validation

George Onyango Orido [a,b,*], Erick Kiplangat Ronoh [a], Patrick Ochuodho Ajwang [a], Benson Baari Gathitu [a]

[a] Jomo Kenyatta University of Agriculture and Technology, Agricultural and Biosystems Engineering Department, Kenya
[b] Egerton University, Faculty of Engineering and Technology, Agricultural Engineering Department, Kenya

ARTICLE INFO

Keywords:
Solar-exhaust gas dryer
Fluid-thermal characteristics
Black nightshade seeds
Exhaust gas heat energy

ABSTRACT

A new method of supplementing heat energy in a solar-exhaust gas greenhouse dryer has been experimentally evaluated in this paper. An internal combustion engine using diesel produced exhaust gas which was channeled to a hybrid recuperative heat exchanger (HRHE) for energy recovery. Fluid and thermal characteristics of the dryer were reported for three modes of drying: solar mode (SM), solar-exhaust gas mode (SEGM), and exhaust gas mode (EGM). Consequently, the dryer room air temperature were found as: 14.82–58.46 °C, 34.49–61.97 °C and 25.75–30.77 °C respectively. Moisture evaporated as a result of temperature variations were computed as: 0–20.8 g, 0–17.79 g and 0–22.33 g respectively. Fluid characteristics of exhaust gas included: average density of 0.7218 kg/m^3, volumetric flow rates from 4.2×10^{-3} – 1.67×10^{-2} m^3/s, maximum residence time of 418 s in HRHE, mass flow rates from 11.32 to 45.07 kg/h, velocity in connectors ranging from 2.14 to 8.52 m/s, velocity in tubes from 0.035 to 0.14 m/s, Reynolds number ranging from 2681 to 10674 in connectors and 344–1368 in tubes, Nusselt number ranging from 14 to 43 in connectors and constant at 3.66 in tubes. Available energy in exhaust gas was found in the range of 2082.32–16002.5 kJ/h, corresponding to temperatures of 197.19–359.82 °C as a result of engine speeds varied from 750 to 2500 rpm. Kinetic energy in exhaust gas increased with increased velocity for both tubes and connectors to a maximum of 39.79 kJ/h in connectors and 1.289×10^{-2} kJ/h in tubes. The significance of this study is in promotion of faster product drying in SEGM and slower drying for delicate products requiring low heat energy supply in EGM.

1. Introduction

Fuel costs have significantly increased due to diminishing supplies of fossil fuel products to industrial and agricultural sectors. Exploring solar energy use remains an alternative in drying of agricultural products, however, in Africa, rainy seasons are characterized by low solar energy intensity and high relative humidity, unsuitable conditions for open sun drying [1]. This necessitates for a supplemental energy source, which in this study, has been experimentally supplied in the form of heat energy from exhaust gas of a diesel engine. Farmers use diesel engines to power hammer mills, unfortunately, heat energy from exhaust gas is released to the environment during milling operations.

Black nightshade, a traditional leafy vegetable is native to Africa and has been traditionally cultivated and consumed in Kenya. The vegetable is an important part of local diets and is valued because of its good response to inputs such as fertilizers and irrigation, high return per unit area, adaptability and richness in vitamins and minerals. In this study, black nightshade seeds were dried using heat energy harvested from exhaust gas of a diesel engine. Black nightshade has been identified as an important crop that has potential for improving food and nutrition security, as well as provision of income to small-holder farmers. Black nightshade vegetable crop is a prioritized agricultural value chain in Kenya and lack of continuous seeds processing (drying) for biodiversity preservation emerged as a gap identified and filled through this study. An economical way to fill the gap was to develop a solar-exhaust gas greenhouse dryer to utilize, besides solar energy, waste heat energy from exhaust gas of a diesel engine which under normal circumstances is lost to the environment. The need for continuous drying and the benefit of reduced drying time of black nightshade seeds has been supported in this study. Kenya demographic and health survey, 2022 has shown that 18 percent of children under five years are stunted, an indication of under-nutrition. Enhanced food safety through preservation of black nightshade seeds is one of the solutions to under-nutrition problem. Given its

* Corresponding author. Jomo Kenyatta University of Agriculture and Technology, Agricultural and Biosystems Engineering Department, Kenya.
E-mail address: george.orido@egerton.ac.ke (G.O. Orido).

https://doi.org/10.1016/j.rineng.2024.102205
Received 1 February 2024; Received in revised form 4 April 2024; Accepted 29 April 2024
Available online 4 May 2024

Nomenclature

A	Area (m^2)
C	Specific heat capacity (kJ/kg • °C)
C_{therm}	Thermal capacitance
D	Diameter (m)
E	Total energy (kJ/h)
ε/D	Ratio of pipe's roughness to diameter
F	Fraction of solar radiation
f	Friction factor
G_1	Constant
G_2	Constant
g	Acceleration due to gravity (m/s^2)
h_{ex}	Position in relation to exhaust gas manifold (m)
h_l	Total head loss (m)
h_f	Frictional head loss (m)
h_m	Minor head loss (m)
h	Convection heat transfer coefficient (W/m^2 • °C)
I	Solar intensity (W/m^2)
I_{effB}	Rate of thermal energy received at black nightshade seeds surface
I_{effG}	Rate of thermal energy received at floor surface of greenhouse dryer
I_{effR}	Rate of thermal energy received by greenhouse dryer air
K	Loss coefficient
k	Thermal conductivity (W/m • °C)
KE	Kinetic energy (kJ/h)
KE_1	Kinetic energy at inlet (kJ/h)
KE_2	Kinetic energy at outlet (kJ/h)
L	Length (m)
M	Moisture content
$\dot{m}$	Mass flow rate (kg/h)
m	Mass (kg)
NV	Number of air exchanges per hour
n	Direction normal to area
P	Pressure (kN/m^2)
Pr	Prandtl number
PE	Potential energy (kJ/h)
PE_1	Potential energy at inlet (kJ/h)
PE_2	Potential energy at outlet (kJ/h)
$\dot{Q}$	Volumetric flow rate (m^3/s)
$\dot{Q}_{conv}$	Rate of convective heat transfer (kJ/h)
$\dot{Q}_{cond}$	Rate of conduction heat transfer (kJ/h)
$\dot{Q}_e$	Rate of heat utilized to evaporate moisture
Re	Reynolds number
R_{therm}	Thermal resistance
r_i	Inner radius (m)
r_o	Inner radius (m)
S_A	Surface area (m^2)
T	Temperature (°C)
t	Time (h)
U	Internal energy (kJ/h)
U_i	Overall heat loss
u	Energy per unit mass (kJ/h)
V	Velocity (m/s)
$WD_{1\rightarrow2}$	Work done by external forces from inlet to outlet (kJ/h)
$\dot{W}_P$	Rate of work done by pressure forces (kJ/h)

Greek letters

Δ	Change
α	Absorptivity
γ	Relative humidity
ζ	Greenhouse dryer room air temperature model parameter
λ	Latent heat of vapourization (kJ/kg)
μ	Dynamic viscosity (N • s/m^2)
ξ	Black nightshade seeds temperature model parameter
ϖ	Random error parameter in black nightshade seeds temperature model
ρ	Density (kg/m^3)
ϱ	Random error parameter in greenhouse dryer room air temperature model
τ	Transmissivity
Ω	Moisture evaporated model parameter

Subscripts

a	Ambient
b	Black nightshade seeds
C	Conservative forces
CN	Connector location
$cond$	Conduction
$conv$	convective
$crit$	Critical
$calc$	Calculated
ES	Engine speed
e	Evaporative
ex	Exhaust gas
$expt$	Experimental
ev	Evaporated
$g\infty$	Floor to underground
gr	Floor to room air
g	Floor
i	Walls and roof
NC	Non conservative forces
n	Floor and tray area
$pred$	Predicted
r	Room air
s	Surface
TB	Tube location
$therm$	Thermal
v	Humid air
$\|_{x=0}$	Floor surface

Abbreviations

ANOVA	Analysis of variance
CN	Connector
EGM	Exhaust gas mode
ExGHDT-SM	Experimental greenhouse dryer temperature in solar mode
ExGHDT-SEGM	Experimental greenhouse dryer temperature in solar-exhaust gas mode
ExGHDT-EGM	Experimental greenhouse dryer temperature in exhaust gas mode
ExME-SM	Experimental moisture evaporated in solar mode
ExME-SEGM	Experimental moisture evaporated in solar-exhaust gas mode
ExME-EGM	Experimental moisture evaporated in exhaust gas mode
HRHE	Hybrid recuperative heat exchanger
HEX	Heat exchanger
LSD	Fisher's least significant difference
MFR	mass flow rate of exhaust gas
NCN	Nusselt number in connectors
NTB	Nusselt number in tubes
ORC	Organic Rankine cycle
ODE	Ordinary differential equations
PDE	Partial differential equations
PrGHDT-SM	Predicted greenhouse dryer temperature in solar mode
PrGHDT-SEGM	Predicted greenhouse dryer temperature in solar-exhaust gas mode
PrGHDT-EGM	Predicted greenhouse dryer temperature in exhaust

gas mode	
PrME-SM	Predicted moisture evaporated in solar mode
PrME-SEGM	Predicted moisture evaporated in solar-exhaust gas mode
PrME-EGM	Predicted moisture evaporated in exhaust gas mode
SM	Solar mode
SEGM	Solar exhaust gas mode
TB	Tube
VEGTB	Velocity of exhaust gas in tubes
VEGCN	Velocity of exhaust gas in connectors

high nutrition profile, consumed in adequate quantities, the traditional leafy vegetable has a potential of addressing the nutritional challenges that Kenya face. In this study, use of HRHE has been reported as a new strategy to enhance energy efficiency and embed sustainability in farm operations that use stationary diesel engines.

Jain and Tiwari [2] presented mathematical models to study thermal behaviour of products under natural convection solar drying with a conclusion that predicted values were in good agreement with experimental observations. Industrialization has led to continuous growth in power demand, and this calls for sustainable means of extracting energy [3] that leaves no environmental impact. However, among the energy sources being implemented, fossil fuels remain the leading option [4–6] to meet the energy demand of the global market. Al-Weheibi et al. [7] carried out numerical investigations on three-dimensional free convective heat transmission flow in a bidisperse permeable matrix within a cubical cavity and concluded that the study's findings might be used in developing heating systems. There has been a lot of heat transfer research and its extensive application in engineering [8–11]. Notwithstanding, among power generation technologies, internal combustion engines have widespread applications in the field of agriculture in milling operations [12]. Concerns over climate change, however, calls for the need of promising technologies such as potential recovery of waste heat for useful applications [13–15] and utilizing clean energy that comes from natural source or replenished sources [16]. According to Sun et al. [17], with depletion of fossil fuel sources and increasing power demands, finding power systems with higher efficiency and lower environmental impact are of major concerns.

The objectives of the current study were to: develop mathematical models for environmental simulation of a solar-exhaust gas greenhouse dryer, use computer simulation to solve the developed models and use experimental data from a physically developed solar-exhaust gas greenhouse dryer to test, verify and validate the developed models based on fluid and thermal characteristics of the dryer. Mathematical modelling and simulation were done based on temperature response, moisture evaporated and constructional parameters that affect the dryer system. Experimental validation need emanated from challenges of computational fluid dynamics of convective heat transfer in an irregular rough walled HRHE with flows at higher Reynolds numbers. The need for simple models to describe responses obtained from controlled products drying experiments has been emphasized because greenhouse drying analysis is complex and is under the influence of external variables in interaction with one another. Results demonstrate a reasonable agreement between experimental and predicted temperatures and moisture evaporated in the dryer. Literature review as per the authors' knowledge reveals no experimental study addressed on fluid and thermal characteristics of a solar-exhaust gas greenhouse dryer. This study therefore fills the gap in addition to its importance in the provision of supplemental energy for product drying.

2. Materials and methods

2.1. Description of study site, system layout and instrumentation for data acquisition

Field experiments were set up at the Department of Agricultural and Biosystems Engineering, Jomo Kenyatta University of Agriculture and Technology (JKUAT), Kenya. The latitude and longitude of the University are 1°5′20.8″ S and 37°0′30″ E, while the altitude is 1527 m above the sea level. The mean annual temperature is 19.85 °C with a mean annual maximum temperature of 24.91 °C and a mean annual minimum temperature of 14.79 °C. The relative humidity range from 15 to 80 %. The climate for the study site is considered warm and temperate with an annual bimodal rainfall of 1014 mm characterized by cold rainy seasons occurring from April to August and October to December each year [18].

To study the variation of temperature and relative humidity profiles inside and outside the solar-exhaust gas greenhouse dryer, twenty-six (AM2301A, China) temperature and relative humidity composite sensors with calibrated digital signal output were used. The sensors performance based on temperature characteristics were resolution ratio of 0.1 °C, accuracy of ± 0.5 °C, measuring range of -40-80 °C and repeatability of 0.2 °C. Based on humidity characteristics, the sensors performance was resolution of 0.1 %, extended measuring range with a minimum of 0 % and a maximum of 99.9 %, accuracy of ± 0.3 %, repeatability of ± 1 %, and hysterisis of ± 0.3 %. Twenty-four of the sensors were placed at the desired locations inside the dryer while one RH sensor and another temperature sensor were placed outside the solar-exhaust gas greenhouse dryer. Surface temperatures of connectors and tubes of the hybrid-recuperative heat exchanger were measured using twelve (DS18B20, China) programmable resolution 1-wire digital thermometers with operating temperature range of −55 °C to +125 °C (± 0.1). With reference to the solar-exhaust gas greenhouse dryer, inside and outside radiations were measured using two (MAX44009, China) ambient light sensors with digital outputs ideal for applications and operations in the dryer. The (AM2301A, China), (DS18B20, China), and (MAX44009, China) sensors were programmed to record data in a microcontroller (ATmega2560, Italy). The Arduino Mega microcontroller was equipped with a 2 GB microSD card for data storage of the drying experiments conducted between July 2022 and January 2023—the ideal period to perform experiments when the weather conditions were most suitable for solar mode, solar-exhaust gas mode, and exhaust gas mode. Mass of black nightshade seeds was recorded after 1 h interval—until no further change in mass occurred—using a strain gauge based digital weighing scale (D-72336 Balingen, Germany) with a precision of ± 0.001 g.

The solar-exhaust gas environment in this study is a dynamic system such that its response is predictable when subjected to a defined input (introduction of heat energy from the sun and diesel engine generated exhaust gas). An internal combustion engine using diesel produces exhaust gas which is channeled to a hybrid recuperative heat exchanger (HRHE) for energy recovery. The HRHE system is at a steady state when the pressure of exhaust gas immediately leaving the engine is increased, forcing the gas through a connector of 0.05 m diameter and into a tube of 0.39 m diameter. A series of six connectors and six tubes are arranged to compose the HRHE as shown in Fig. 1 such that an increase of exhaust gas mass in the tubes leads to an increase in pressure. The exit pipe of the HRHE is open to the atmosphere leading to a zero-gauge pressure and in two ways, energy is added to or subtracted from the HRHE. Energy in the form of exhaust gas internal energy, kinetic energy, and potential energy is transported into or out of the hybrid recuperative heat exchanger through its boundaries (inlet and outlet). In addition, energy is transferred to the hybrid recuperative heat exchanger surface in the form of heat when the dryer is operated on solar-exhaust gas mode.

The properties of the solar-exhaust gas system, that is, density of exhaust gas, temperature of drying air and that of the working fluid, change due to transport of mass. Heat transfer processes in this dynamic system involve the transport of energy from the exhaust gas to the HRHE

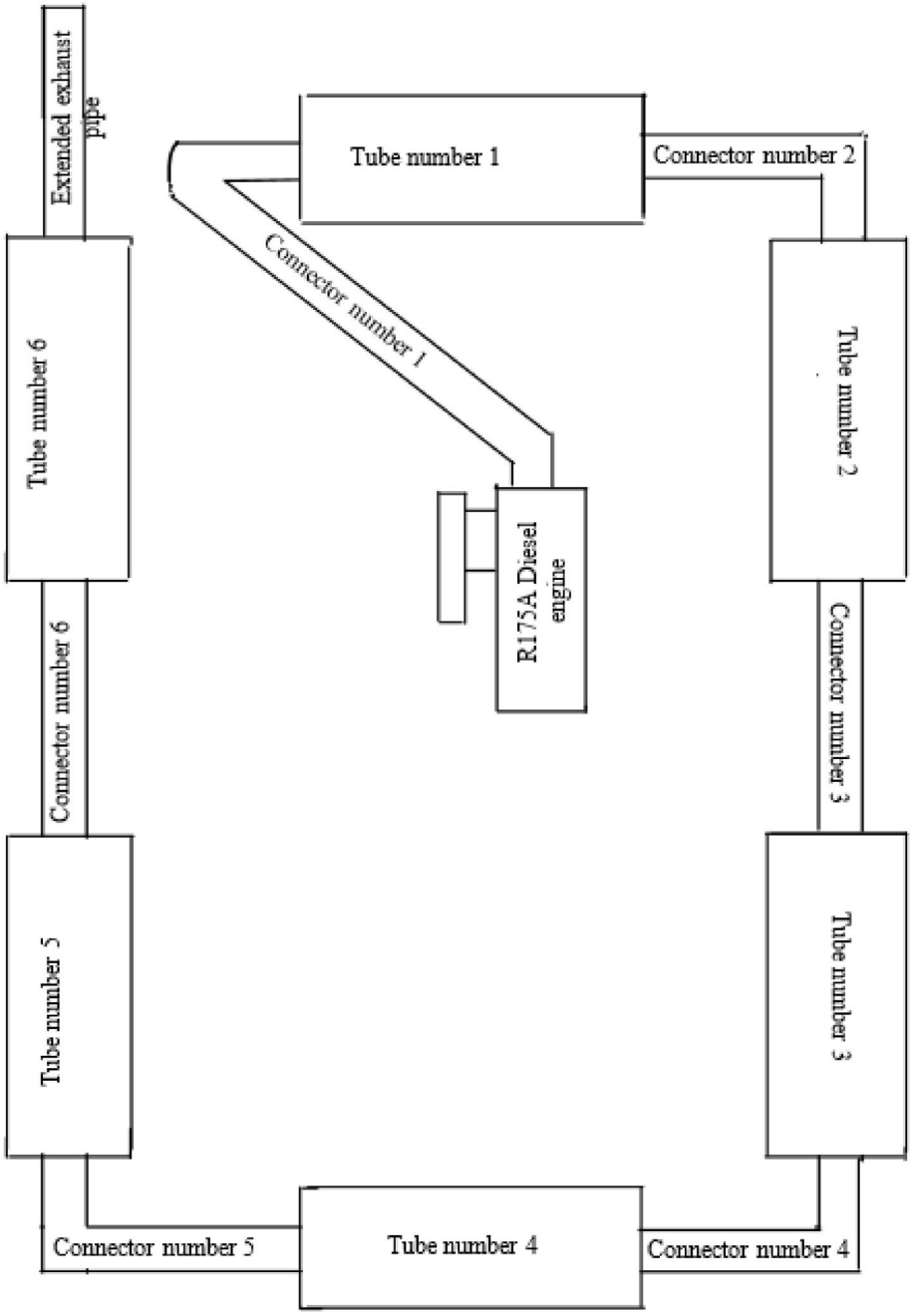

Fig. 1. Schematic arrangement of cylindrical tubes to connectors to form HRHE.

surface. The analyses of fluid and thermal systems of the solar-exhaust gas dryer use the assumption of lumped parameter such that all dependent variables and properties are constant in relation to space and size with time being the independent variable. A pictorial view of the HRHE is shown in Fig. 2 and the layout of the HRHE inside a solar-exhaust gas greenhouse dryer is shown in Fig. 3. Mature black nightshade berries (Fig. 4) were harvested (Fig. 5) and seeds were extracted (Fig. 6) and dried (Fig. 7) to a final product (Fig. 8) ready for storage or planting.

2.2. Principle of work and energy as applied to modelling exhaust gas flow

The work and energy principle is derived by taking the dot product of Newton's second law of motion. Both sides of the resulting equation were integrated while considering the path of motion of exhaust gas from inlet to outlet of HRHE. The general form of the principle of work and energy is expressed in Eq. (1).

$$KE_2 = KE_1 + WD_{1\to 2} \tag{1}$$

In Eq. (1), KE_2 is the kinetic energy of the exhaust gas at heat exchanger outlet, KE_1 is the kinetic energy at inlet, $WD_{1\to 2}$ is the work done by all external forces as the exhaust gas moves from the inlet denoted by 1 to the outlet denoted by 2, in the heat exchanger. The potential energy function, PE, is defined for both conservative and non-conservative forces where conservative forces had their work dependent on the initial and final positions of the exhaust gas and non-conservative forces had their work dependent on the path of motion of the exhaust gas as it flowed through the heat exchanger. In both cases, the potential energy function is defined so that the work done is expressed as a difference in potential energies as shown in Eq. (2) where PE_1 is the potential energy

Fig. 2. Pictorial view of the hybrid recuperative heat exchanger [1,4,18].

of the exhaust gas at heat exchanger inlet, PE_2 is the potential energy at outlet.

$$WD_{1\to2} = PE_1 - PE_2 \tag{2}$$

Consequently, the total work is represented using Eq. (3). In the equation, conservative forces were denoted by C, and non-conservative forces were denoted by NC.

$$WD_{1\to2} = (WD_{1\to2})_C + (WD_{1\to2})_{NC} \tag{3}$$

The total energy in the exhaust gas is the sum of kinetic and potential energies which for a conservative system is constant and satisfies the principle of conservation of energy as shown in Eq. (4).

$$KE_{ex} + PE_{ex} = Constant \tag{4}$$

In Eq. (4), KE_{ex} is the exhaust gas kinetic energy and PE_{ex} is the exhaust gas potential energy. For the purposes of direct application, Eq. (4) is used to develop its equivalence as shown in Eq. (5).

$$\frac{1}{2}\dot{m}_{ex}V_{ex}^2 + \dot{m}_{ex}.g.h_{ex} = Constant \tag{5}$$

In Eq. (5), $\dot{m}_{ex}$ is the mass flow rate of exhaust gas, V_{ex} is the exhaust gas velocity, g is the acceleration due to gravity, and h_{ex} is the position of

Fig. 4. Mature black nightshade berries on plant.

Fig. 5. Freshly harvested black nightshade berries ready for seeds extraction.

Fig. 3. Layout of the HRHE in solar-exhaust gas dryer.

Fig. 6. Extraction of seeds from black nightshade berries.

exhaust gas in relation to the exhaust gas manifold. In the current application the potential energy is insignificant.

2.3. Conservation of exhaust gas mass analysis in the heat exchanger

The control volume form of conservation of mass in a HRHE in which exhaust gas flows is given in Eq. (6).

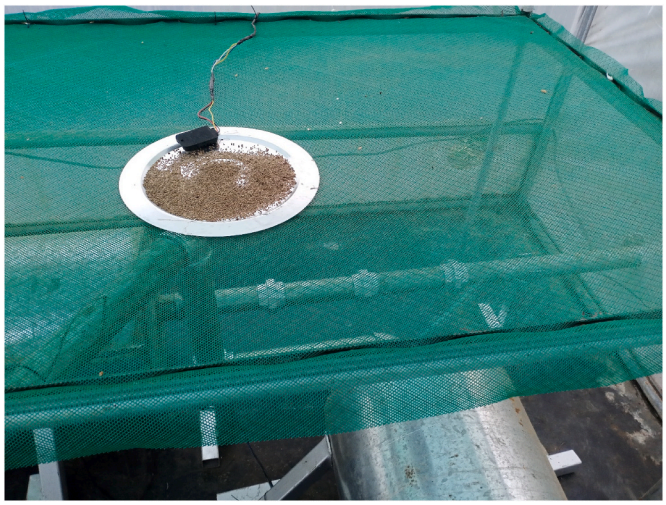

Fig. 7. Drying of black nightshade seeds in a solar-exhaust gas greenhouse dryer.

$$\begin{pmatrix} \text{Rate at which} \\ \text{mass enters} \\ \text{heat exchanger} \end{pmatrix} - \begin{pmatrix} \text{Rate at which} \\ \text{mass leaves} \\ \text{heat exchanger} \end{pmatrix} = \begin{pmatrix} \text{Rate at which} \\ \text{mass accumulates in} \\ \text{heat exchanger} \end{pmatrix} \tag{6}$$

Mass enters and leaves the heat exchanger through its boundaries (inlet and outlet). The rate at which mass crossed the boundary of the heat exchanger is the mass flow rate of exhaust gas, $\dot{m}_{ex}$. If m_{ex} is the total mass of exhaust gas in the heat exchanger at any instant, Eq. (6) is written as Eq. (7).

$$\dot{m}_{ex.\ in} - \dot{m}_{ex.\ out} = \frac{dm_{ex}}{dt} \tag{7}$$

The total mass of exhaust gas in the heat exchanger at any instant is as given in Eq. (8).

$$m_{ex} = \int \rho_{ex} dV_{HEX} \tag{8}$$

In Eq. (8), ρ_{ex} is the mass density of exhaust gas and V_{HEX} is the volume of the heat exchanger. The mass flow rate of exhaust gas is written as shown in Eq. (9).

$$\dot{m}_{ex} = \rho_{ex} \bullet \dot{Q}_{ex} \tag{9}$$

In Eq. (9), $\dot{Q}_{ex}$ is the volumetric flow rate of exhaust gas. Using Eq. (8) and Eq. (9) in Eq. (7) yields Eq. (10).

$$\rho_{ex.\ in} \bullet \dot{Q}_{ex.\ in} - \rho_{ex.\ out} \bullet \dot{Q}_{ex.\ out} = \frac{d}{dt}\left(\int \rho_{ex} dV_{HEX}\right) \tag{10}$$

Exhaust gas entering the heat exchanger is assumed to be of a constant species, homogenous, and the density did not vary with time so that, $\rho_{ex} = \rho_{ex.\ in} = \rho_{ex.\ out}$. Consequently, Eq. (10) reduced to Eq. (11).

$$\dot{Q}_{ex.\ in} - \dot{Q}_{ex.\ out} = \frac{dV_{HEX}}{dt} \tag{11}$$

2.4. Modeling total energy in the HRHE

The total energy in the control volume (hybrid recuperative heat exchanger) is given by Eq. (12).

$$E_{HEX} = U_{ex} + KE_{ex} + PE_{ex} + E_{other} \tag{12}$$

In Eq. (12), E_{HEX} is the total energy in the heat exchanger, U_{ex} is the internal energy of all particles in the heat exchanger, KE_{ex} is the exhaust

gas kinetic energy, PE_{ex} is the exhaust gas potential energy, and E_{other} represents other forms of energy such as energy stored in the components and energy associated with any reactions within the heat exchanger. The potential energy in the exhaust and other forms of energy were insignificant in our control volume, therefore, Eq. (12) is reduced to Eq. (13).

$$E_{HEX} = U_{ex} + KE_{ex} \tag{13}$$

To obtain the total internal energy, the specific energy (the energy per unit mass, u_{ex} , over the control volume) is integrated as shown in Eq. (14).

$$U_{ex} = \int u_{ex} dm_{ex} = \int u_{ex}\, \rho_{ex} dV_{HEX} \tag{14}$$

In Eq. (14), m_{ex} is the mass of exhaust gas, ρ_{ex} is the mass density of exhaust gas and V_{HEX} is the volume of the heat exchanger. Internal energy is the energy associated with the random motion of exhaust gas molecules and thus is a function of temperature. The specific internal energy associated with the exhaust gas flow is given by Eq. (15).

$$u_{ex} = C_{ex} T_{ex} \tag{15}$$

In Eq. (15), C_{ex} is the specific heat capacity of exhaust gas and T_{ex} is the temperature of the exhaust gas. Using these definitions, Eq. (13) is rewritten as Eq. (16).

$$E_{HEX} = \int (KE_{ex} + u_{ex}\rho_{ex}) dV_{HEX} \tag{16}$$

The form of the energy equation for the heat exchanger as a control volume is summarized in Eq. (17).

$$\begin{pmatrix} Rate\ at\ which\ energy\ is\ transferred\ into\ the\ heat\ exchanger\ through\ its\ boundaries \end{pmatrix} - \begin{pmatrix} Rate\ at\ which\ energy\ is\ transferred\ out\ of\ the\ heat\ exchanger\ through\ its\ boundaries \end{pmatrix} + \begin{pmatrix} \text{Rate of convection heat transfer to the surface of the heat exchanger} \end{pmatrix} = \begin{pmatrix} Rate\ at\ which\ energy\ accumulates\ within\ the\ heat\ exchanger \end{pmatrix} \tag{17}$$

The HRHE used in the current study had one inlet and one outlet, therefore, Eq. (17) is rewritten as Eq. (18).

$$\dot{m}_{ex.\ in}(u_{ex} + KE_{ex})_{in} - \dot{m}_{ex.\ out}(u_{ex} + KE_{ex})_{out} + \dot{Q}_{conv} = \frac{d}{dt}\left[\int (KE_{ex} + u_{ex}\rho_{ex}) dV_{HEX}\right] \tag{18}$$

In Eq. (18), $\dot{m}_{ex.\ in}$ is the mass flow rate of exhaust gas at the inlet of the heat exchanger, $\dot{m}_{ex.\ out}$ is the mass flow rate at the outlet and $\dot{Q}_{conv}$ is the rate of convection heat transfer to the surface of the heat exchanger.

Assuming steady flow of exhaust gases, the rate of work done by pressure forces is given by Eq. (19).

$$\dot{W}_P = \left(\dot{m}_{ex}\frac{P_{ex}}{\rho_{ex}}\right)_{in} - \left(\dot{m}_{ex}\frac{P_{ex}}{\rho_{ex}}\right)_{out} \tag{19}$$

In Eq. (19), $\dot{W}_P$ is the work done by pressure forces, and P_{ex} is the exhaust gas pressure. Using Eq. (19) in Eq. (18) resulted in Eq. (20), which is the form of the energy equation for the HRHE with one inlet and one outlet as utilized in the present work.

$$\dot{m}_{ex.\ in}\left(u_{ex} + \frac{P_{ex}}{\rho_{ex}} + KE_{ex}\right)_{in} - \dot{m}_{ex.\ out}\left(u_{ex} + \frac{P_{ex}}{\rho_{ex}} + KE_{ex}\right)_{out} + \dot{Q}_{conv} = \frac{d}{dt}\left[\int (KE_{ex} + u_{ex}\rho_{ex}) dV_{HEX}\right] \tag{20}$$

2.5. Application of Bernoulli's equation for exhaust gas flow in the HRHE

For the flow of exhaust gas in the hybrid recuperative heat exchanger, Eq. (21) is applied.

$$\frac{P_{ex.\ in}}{\rho_{ex}} + \frac{V^2_{ex.\ in}}{2} + PE_{ex.\ in} = \frac{P_{ex.\ out}}{\rho_{ex}} + \frac{V^2_{ex.\ out}}{2} + PE_{ex.\ out} \tag{21}$$

In Eq. (21), $P_{ex.\ in}$ and $P_{ex.\ out}$ are the inlet and outlet pressures of exhaust gas, $V_{ex.\ in}$ and $V_{ex.\ out}$ are the inlet and outlet velocities of exhaust gas, $PE_{ex.\ in}$ and $PE_{ex.\ out}$ are the inlet and outlet potential energies, and ρ_{ex} is the exhaust gas density. In the present work, the exhaust gas potential energy is insignificant, therefore, Eq. (21) reduced to Eq. (22).

$$\frac{P_{ex.\ in}}{\rho_{ex}} + \frac{V^2_{ex.\ in}}{2} = \frac{P_{ex.\ out}}{\rho_{ex}} + \frac{V^2_{ex.\ out}}{2} \tag{22}$$

Under the assumptions of steady flow, the HRHE energy equation represented by Eq. (20) reduced to Eq. (23).

$$\dot{m}_{ex.\ in}\left(u_{ex} + \frac{P_{ex}}{\rho_{ex}} + KE_{ex}\right)_{in} - \dot{m}_{ex.\ out}\left(u_{ex} + \frac{P_{ex}}{\rho_{ex}} + KE_{ex}\right)_{out} + \dot{Q}_{conv} = 0 \tag{23}$$

For steady flow of exhaust gas, there is no mass accumulation within the heat exchanger, such that, $\dot{m}_{ex} = \dot{m}_{ex.\ in} = \dot{m}_{ex.\ out}$. Dividing Eq. (23) by $\dot{m}_{ex}$ and defining $q_{ex} = \dot{Q}_{conv}/\dot{m}_{ex}$, Eq. (23) reduced to Eq. (24).

$$\left(u_{ex} + \frac{P_{ex}}{\rho_{ex}} + KE_{ex}\right)_{in} - \left(u_{ex} + \frac{P_{ex}}{\rho_{ex}} + KE_{ex}\right)_{out} + q_{ex} = 0 \tag{24}$$

Fig. 8. Dried black nightshade seeds ready for storage or planting.

If the following three equations are applied to Eq. (24):

$$q_{ex} = u_{ex.\ out} - u_{ex.\ in} \tag{25}$$

$$(KE_{ex})_{in} = \frac{V^2_{ex.\ in}}{2} \tag{26}$$

$$(KE_{ex})_{out} = \frac{V^2_{ex.\ out}}{2} \tag{27}$$

It follows that Eq. (24) reduced to Bernoulli's equation as defined in Eq. (22), which is applicable for the flow of exhaust gas in the HRHE used in the current work. Eq. (25) implied that heat transferred to the heat exchanger led to an increase of internal energy. In addition, Eq. (22) involved the term $(P_{ex.\ in} - P_{ex.\ out})/\rho_{ex}$ which is the gauge pressure and exposing the exhaust gas flow to the open atmosphere made the gauge pressure to be zero.

2.6. Determination of losses in the HRHE pipe flow system

The total head loss in the hybrid recuperative heat exchanger piping system is given using Eq. (28).

$$h_l = h_f + h_m \tag{28}$$

In Eq. (28), h_l is the total head loss, h_f is the head loss due to friction (major head losses), and h_m is the sum of all minor head losses due to elbows, unions, sockets, and connectors used in the piping system. Connectors caused sudden contraction in the HRHE. Minor head losses were expressed in the form of Eq. (29).

$$h_m = K\frac{V^2_{ex}}{2g} \tag{29}$$

In Eq. (29), K is a loss coefficient, V_{ex} is the exhaust gas velocity, and g is the acceleration due to gravity. The frictional head loss in the heat exchanger piping system is dependent on the geometry of the pipe as well as the flow properties and it is expressed in the form of Eq. (30).

$$h_f = f\frac{L}{D}\frac{V^2_{ex}}{2g} \tag{30}$$

In Eq. (30), f is the friction factor, L is either the length of a tube or connector, and D is either the diameter of a tube or connector. The friction factor is defined as a function of two dimensionless parameters expressed in Eq. (31).

$$f = function\left(Re, \frac{\varepsilon}{D}\right) \tag{31}$$

In Eq. (31) ε/D is the ratio of the pipe's roughness to its diameter. The Reynolds number, Re is defined as expressed in Eq. (32) [19].

$$Re = \frac{\rho_{ex} \bullet V_{ex} \bullet D}{\mu_{ex}} \tag{32}$$

In Eq. (32), Re is the dimensionless Reynolds number, ρ_{ex} is the exhaust gas density, and μ_{ex} is the dynamic viscosity of exhaust gas. For laminar flow in tubes of the heat exchanger, analytical methods were used to show that the friction factor is expressed as shown in Eq. (33).

$$f = \frac{64}{Re} \tag{33}$$

Noting that the velocity of exhaust gas in a circular pipe is related to the volumetric flow rate [20], Eq. (33) is expressed as:

$$V_{ex} = \frac{4\dot{Q}_{ex}}{\pi D^2} \tag{34}$$

The substitution of Eq. (32) and Eq. (33) into Eq. (30) led to Eq. (35), which is used for laminar flows in tubes.

$$h_f = \frac{128 \bullet \mu_{ex} \bullet L}{\rho_{ex} \bullet g \bullet \pi \bullet D^4}\ \dot{Q}_{ex} \tag{35}$$

The Colebrook equation provided a quantitative fit to empirical data for a pressure drop in the heat exchanger pipe system and it is used as an empirical method to quantify Eq. (31) for turbulent flows in connectors as expressed in Eq. (36).

$$\frac{1}{\sqrt{f}} = -2.0\ log\left(\frac{\varepsilon}{3.7D} + \frac{2.51}{Re\sqrt{f}}\right) \tag{36}$$

Consequently, because it is not possible to solve Eq. (36) in closed form to determine the friction factor after obtaining the values of Reynolds number and the ratio of the pipe's roughness to its diameter, the friction factor is obtained by referring to the Moody diagram, a chart that provided curves of friction factors versus Reynolds number for different values of the ratio of the pipe's roughness to its diameter. Galvanized iron, an ideal metal for fabrication and welding using tungsten inert gas (TIG) welding technique was used to fabricate the HRHE. From the Moody diagram, the ratio of pipe's roughness to its diameter for galvanized iron connectors of 50 mm diameter was used as 0.003 and for the tubes of 390 mm the ratio was 0.0004. Major head losses due to friction were determined and reported, while minor head losses in the piping system were considered insignificant.

2.7. Thermal modeling of the HRHE system

Internal energy is accumulated in the heat exchanger before it is dissipated to the solar-exhaust gas greenhouse dryer environment. The thermal capacitance of the heat exchanger is defined as expressed in Eq. (37).

$$C_{therm} = \frac{dU_{ex}}{dT_{ex}} \tag{37}$$

In Eq. (37), C_{therm} is the thermal capacitance of the heat exchanger, U_{ex} is the total internal energy in the exhaust gas, and T_{ex} is the exhaust gas temperature. The heat transfer to the heat exchanger surface from the exhaust gas is resisted with a thermal resistance defined in Eq. (38).

$$R_{therm} = \frac{\Delta T_{ex}}{\dot{Q}_{conv}} \tag{38}$$

In Eq. (38), R_{therm} is the thermal resistance, ΔT_{ex} is the temperature difference between the exhaust gas and heat exchanger surface, and $\dot{Q}_{conv}$ is the convective heat transfer rate between them. The total internal energy, U_{ex} , is a product of the mass of exhaust gas, m_{ex} , and the specific internal energy, u_{ex}. From Eq. (15), the specific internal energy is equal to the product of specific heat capacity of exhaust gas, C_{ex} , and the temperature, T_{ex}. The application of Eq. (37) led to the thermal capacitance of the heat exchanger as expressed in Eq. (39).

$$C_{therm} = m_{ex} \bullet C_{ex} \tag{39}$$

The transient behaviour of the heat exchanger is modeled by applying conservation of energy to the exhaust gas. Energy, in the form of heat, is transferred to the surface of the heat exchanger and the rate of change of internal energy is equal to the rate at which heat is transferred to the heat exchanger surface as defined in Eq. (40).

$$\frac{dU_{ex}}{dt} = \dot{Q}_{conv} \tag{40}$$

With the assumption of constant specific heat and using Eq. (38), Eq. (40) becomes as expressed in Eq. (41).

$$m_{ex}C_{ex}\frac{dT_{ex}}{dt} = -\frac{1}{R_{therm}}(T_{ex} - T_s) \tag{41}$$

In Eq. (41), T_s is the heat exchanger surface temperature. Eq. (41) is

rearranged and expressed as Eq. (42) which is a first order differential equation.

$$m_{ex}C_{ex}\frac{dT_{ex}}{dt}+\frac{1}{R_{therm}}T_{ex}=\frac{1}{R_{therm}}T_s \tag{42}$$

In as much as conduction heat transfer in the current work is insignificant because the inside and outside heat exchanger surface temperatures were assumed to be the same over a 1.6 mm thickness of galvanized iron making tubes and connectors, the rate of heat transfer through conduction could be modeled by Fourier's law of conduction as expressed in Eq. (43).

$$\frac{\dot{Q}_{cond}}{S_A}=-k\frac{\partial T_{ex}}{\partial n} \tag{43}$$

In Eq. (43), $\dot{Q}_{cond}$ is the conduction heat transfer rate, S_A is the surface area, k is the thermal conductivity and, n is the direction normal to the area through which heat is transferred. The resistance due to conduction in the annular cylindrical heat exchanger of length, inner radius, r_i , and outer radius, r_o , which was made of galvanized iron of thermal conductivity, k , could be modeled as expressed in Eq. (44).

$$R_{therm}=\frac{1}{2\pi kL}\ln\left(\frac{r_o}{r_i}\right) \tag{44}$$

Convection heat transfer occurred between the moving exhaust gas at high temperature and the heat exchanger surface at rest. A thermal boundary layer, as a thin region near the heat exchanger surface, existed with a temperature gradient, therefore, the rate of convection heat transfer per unit area is modeled by Newton's law of cooling [21] as expressed in Eq. (45).

$$\frac{\dot{Q}_{conv}}{S_A}=h_{conv}(T_{ex}-T_s) \tag{45}$$

In Eq. (45), $\dot{Q}_{conv}$ is the convection heat transfer rate, and h_{conv} is the convection heat transfer coefficient.

2.8. Energy balance models for product drying

Considering black nightshade seeds drying, solar radiation is converted to thermal energy. According to Jain and Tiwari [2] solar radiation falling on the seeds' surface is partly absorbed to evaporate moisture from it to the surrounding air. Plastic cover used in the dryer produces a greenhouse effect by trapping solar energy in the form of thermal heat expressed in Eq. (46) where with respect to greenhouse cover, I_i is solar intensity (W/m^2), A_i is area (m^2) and τ_i is transmissivity.

$$Thermal\ heat\ within\ cover=\sum I_iA_i\tau_i \tag{46}$$

A fraction of trapped energy is received partly by black nightshade seeds and partly by the floor and exposed tray area as shown in Eq. (47) and Eq. (48) while the remaining solar radiation will heat the enclosed air inside the solar-exhaust gas greenhouse dryer as shown in Eq. (49) where α is absorptivity and for Eqs. (47)–(49), F is fraction of solar radiation.

$$Radiation\ received\ by\ black\ nightshade\ seeds=F_b\sum I_iA_i\tau_i \tag{47}$$

$$Radiation\ received\ by\ \ floor\ and\ tray\ area=(1-F_n)\sum I_iA_i\tau_i \tag{48}$$

$$Remaining\ solar\ radiation=(1-F_n)(1-F_b)(1-\alpha_g)\sum I_iA_i\tau_i \tag{49}$$

To write the energy balance equations, the assumptions made were: thin layer drying is adopted, heat capacity of greenhouse dryer cover and wall material is neglected, no stratification in greenhouse dryer air temperature, absorptivity of air is neglected, and greenhouse dryer is east-west oriented [22]. Thermal models for prediction of black nightshade seeds temperature and moisture evaporation were developed using energy balance equations for forced convection drying system in a solar-exhaust gas greenhouse dryer. For the energy balance equation [2,5,9,14,23,24] at black nightshade seeds surface, the form is expressed in Eq. (50) which is then rewritten as Eq. (51).

$$\begin{bmatrix}Rate\ of\ thermal\ energy\ received\ at\ black\ nightshade\ seeds\ surface\end{bmatrix}=\begin{bmatrix}Rate\ of\ thermal\ energy\ stored\ by\ black\ nightshade\ seeds\end{bmatrix}+\begin{bmatrix}Rate\ of\ thermal\ energy\ lost\ due\ to\ convection\ loss\end{bmatrix}+\begin{bmatrix}Rate\ of\ thermal\ energy\ lost\ due\ to\ evaporation\ loss\end{bmatrix} \tag{50}$$

$$(1-F_n)F_b\alpha_b\sum I_iA_i\tau_i=M_bC_b\frac{dT_b}{dt}+h_b(T_b-T_r)A_b+0.016h_b[P(T_b)-\gamma_rP(T_r)]A_b \tag{51}$$

In Eq. (51), F_n is the fraction of solar radiation falling on tray area, F_b is the fraction of solar radiation falling on black nightshade seeds, α_b is the absorptivity of black nightshade seeds, I_i is the solar intensity on greenhouse dryer walls/roof, A_i is the area of greenhouse dryer walls/roof, τ_i is the transmissivity of greenhouse dryer walls/roof, M_b is the moisture content of black nightshade seeds, C_b is the specific heat capacity of black nightshade seeds, T_b is the temperature of black nightshade seeds, h_b is the convective heat transfer coefficient of black nightshade seeds, T_r is the greenhouse dryer room air temperature, A_b is the surface area of black nightshade seeds, P is the vapour pressure, and γ_r is the relative humidity of greenhouse dryer room air. The energy balance equation [2,5,9,14,23,24] at ground surface is summarized in the form of Eq. (52) which is then rewritten as Eq. (53).

$$\begin{bmatrix}Rate\ of\ thermal\ energy\ received\ at\ floor\ surface\end{bmatrix}=\begin{bmatrix}Rate\ of\ thermal\ energy\ lost\ inside\ the\ ground\ due\ to\ conduction\ loss\end{bmatrix}+\begin{bmatrix}Rate\ of\ thermal\ energy\ lost\ from\ floor\ to\ greenhouse\ dryer\ air\ due\ to\ convection\ and\ radiation\ losses\end{bmatrix} \tag{52}$$

$$(1-F_n)(1-F_b)\alpha_g\sum I_iA_i\tau_i=h_{g\infty}\left(T|_{x=0}-T_\infty\right)A_g+h_{gr}\left(T|_{x=0}-T_r\right)\left(A_g-A_b\right) \tag{53}$$

In Eq. (53), F_n is the fraction of solar radiation falling on tray area, F_b is the fraction of solar radiation falling on black nightshade seeds, α_g is the absorptivity of greenhouse dryer floor surface, I_i is the solar intensity on greenhouse dryer walls/roof, A_i is the area of greenhouse dryer walls/roof, τ_i is the transmissivity of greenhouse dryer walls/roof, $h_{g\infty}$ is the convective heat transfer coefficient of greenhouse dryer floor to underground, $T|_{x=0}$ is the temperature of greenhouse dryer floor surface, T_∞ is the underground temperature, h_{gr} is the convective heat transfer coefficient of greenhouse dryer floor to room air, T_r is the greenhouse dryer room air temperature, A_b is the surface area of black nightshade seeds, and A_g is the area of greenhouse dryer floor surface. The energy balance equation [2,5,9,14,23,24] at greenhouse dryer chamber is written by using the number of air exchange per hour and is summarized in the form of Eq. (54) which is then rewritten as Eq. (55). In Eq. (55), F_n is the fraction of solar radiation falling on tray area, F_b is the fraction of solar radiation falling on black nightshade seeds, α_g is the absorptivity of greenhouse dryer floor surface, I_i is the solar intensity on greenhouse dryer walls/roof, A_i is the area of greenhouse dryer walls/roof, τ_i is the transmissivity of greenhouse dryer walls/roof, h_b is the convective heat transfer coefficient of black nightshade seeds, T_b is the temperature of black nightshade seeds, T_r is the greenhouse dryer room air temperature, A_b is the surface area of black nightshade seeds, P is the vapour pressure,

γ_r is the relative humidity of greenhouse dryer room air, h_{gr} is the convective heat transfer coefficient of greenhouse dryer floor to room air, $T|_{x=0}$ is the temperature of greenhouse dryer floor surface, A_g is the area of greenhouse dryer floor surface, T_a is the ambient temperature, and U_i is the overall heat loss on greenhouse dryer walls/roof.

$$\begin{bmatrix}\text{Rate of thermal energy recieved by greenhouse dryer air}\end{bmatrix} + \begin{bmatrix}\text{Rate of thermal energy received from black nightshade seeds due to convection loss}\end{bmatrix} + \begin{bmatrix}\text{Rate of thermal energy received due to evaporation loss from black nightshade seeds}\end{bmatrix} + \begin{bmatrix}\text{Rate of thermal energy received from greenhouse dryer floor due to conduction and radiation losses}\end{bmatrix} = \begin{bmatrix}\text{Rate of thermal energy lost to the ambient air by forced ventilation}\end{bmatrix} + \begin{bmatrix}\text{Rate of overal heat loss from greenhouse dryer air to ambient air through canopy cover}\end{bmatrix} \tag{54}$$

$$(1-F_n)(1-F_b)(1-\alpha_g)\sum I_iA_i\tau_i + h_b(T_b-T_r)A_b + 0.016h_b[P(T_b) - \gamma_r P(T_r)]A_b + h_{gr}\left(T|_{x=0}-T_r\right)\left(A_g-A_b\right) = 0.33NV(T_r-T_a) + \sum U_iA_i(T_r-T_a) \tag{55}$$

$$I_{effB} = (1-F_n)F_b\alpha_b\sum I_iA_i\tau_i \tag{59}$$

$$I_{effG} = (1-F_n)(1-F_b)\alpha_g\sum I_iA_i\tau_i \tag{60}$$

$$I_{effR} = (1-F_n)(1-F_b)\left(1-\alpha_g\right)\sum I_iA_i\tau_i \tag{61}$$

Similarly, Eqs. (62)–(66) are expressed and used in the following formats to solve the mathematical models.

$$H_g = \left[1+\frac{h_{g\infty}A_g}{h_{gr}\left(A_g-A_b\right)}\right]^{-1} \tag{62}$$

$$UA_{g\infty} = \left[\frac{1}{h_{gr}\left(A_g-A_b\right)}+\frac{1}{h_{g\infty}A_g}\right]^{-1} \tag{63}$$

$$P(T) = exp\left[25.317-\frac{5144}{T+273.15}\right] \tag{64}$$

$$h_{be} = h_b + h_r \tag{65}$$

$$h_r = \frac{\varepsilon\sigma\left[(T_b+273.15)^4-(T_v+273.15)^4\right]}{T_b-T_v} \tag{66}$$

With the help of Eqs. (58) and (60) to (63), Eq. (55) is simplified to determine the greenhouse dryer room temperature under forced convection mode for values of black nightshade seeds temperature and ambient temperature as given in Eq. (67).

$$T_r = \frac{I_{effR}+h_bA_bT_b+0.016(G_1T_b+R_2-\gamma_rG_2)+H_gI_{effG}+\left[(UA)_{g\infty}+0.33NV+\sum U_iA_i\right]T_a}{h_bA_b+0.016h_b\gamma_rG_1+(UA)_{g\infty}+0.33NV+\sum U_iA_i} \tag{67}$$

2.9. Solution of energy balance models

Two approximations are used to solve the mathematical models given in Eqs. (50)–(55). First, it is noted that black nightshade seeds area, A_b, reduces with moisture reduction due to shrinkage which leads to a change in absorption of solar energy during drying process. Using shrinkage ratio as a function of moisture ratio allows for approximation of the value of A_b as shown in Eqs. (56) and (57) [25,26].

$$\frac{A_b}{A_{b0}} = 0.339+1.246W_m-1.385W_m^2+0.792W_m^3 \tag{56}$$

$$W_m = \frac{X_m}{X_{m0}} \tag{57}$$

The second approximation is based on linearization of partial vapour pressure, as shown in Eq. (58), over small temperature ranges between 25 and 55 °C in which solar drying mostly occurs.

$$P(T) = G_1T+G_2 \tag{58}$$

If I_{effB} is the rate of thermal energy received at black nightshade seeds surface, I_{effG} is the rate of thermal energy received at floor surface of greenhouse dryer, and I_{effR} is the rate of thermal energy received by greenhouse dryer air, then their expressions and use are as shown in Eqs. (59)–(61).

Substituting linear expression of partial vapour pressure in Eqs. (51) and (55) and combining the resultant equations, a form of a first order differential equation is produced for black nightshade seeds temperature as shown in Eq. (68).

$$\frac{dT_b}{dt}+\psi T_b = f(t) \tag{68}$$

In Eq. (68), the derivative, ψ and the time dependent derivative, $f(t)$ are determined using Eqs. (69) and (70).

$$\psi = \frac{h_bA_b(1+0.016G_1)}{M_bC_b} \tag{69}$$

$$f(t) = \frac{I_{effB}+h_bA_b[T_r-0.016\{G_2-\gamma_r(G_1T_r+G_2)\}]}{M_bC_b} \tag{70}$$

Once the value of the greenhouse dryer room air temperature, T_r is known, with the help of Eq. (51), black nightshade seeds temperature, T_b can be determined using Eq. (68) and the rate of moisture evaporation is evaluated using the expression in Eq. (71).

$$m_{ev} = 0.016\frac{h_b}{\lambda}[(G_1T_b+G_2)-\gamma_r(G_1T_r+G_2)]A_bt \tag{71}$$

2.10. Convective heat transfer coefficient for black nightshade seeds

The Nusselt number is a function of Reynolds and Prandtl numbers

for forced convection [27] as expressed in Eq. (72).

$$Nu = \frac{h_b X}{K_v} = C(RePr)^n \tag{72}$$

The hourly data of relative humidity inside the solar-exhaust gas greenhouse dryer, black nightshade surface temperature, inside the dryer air temperature and mass of black nightshade seeds were recorded during the experiment. The moisture evaporated, m_{ev} is calculated by taking the difference of mass of black nightshade seeds between two consecutive readings at 1-h intervals. The convective heat transfer coefficient of black nightshade seeds, h_b under forced convection mode of drying is defined as shown in Eq. (73) [28].

$$h_b = \frac{K_v}{X} C(RePr)^n \tag{73}$$

The rate of heat utilized to evaporate moisture is given as shown in Eq. (74).

$$\dot{Q}_e = 0.016 h_b [P(T_b) - \gamma_r P(T_r)] \tag{74}$$

On substituting h_b from Eq. (73), Eq. (74) becomes Eq. (75).

$$\dot{Q}_e = 0.016 \frac{K_v}{X} C(RePr)^n [P(T_b) - \gamma_r P(T_r)] \tag{75}$$

Evaporation moisture is determined by dividing Eq. (75) by the latent heat of vapourization, λ and multiplying by the area of black nightshade seeds drying tray, A_b and the time interval, t as expressed in Eq. (76) which is similar to the form of Eq. (71).

$$m_{ev} = \frac{\dot{Q}_e}{\lambda} A_b t = 0.016 \frac{K_v}{X\lambda} C(RePr)^n [P(T_b) - \gamma_r P(T_r)] A_b t \tag{76}$$

Let Eq. (77) be expressed as:

$$Z = 0.016 \frac{K_v}{X\lambda} [P(T_b) - \gamma_r P(T_r)] A_b t \tag{77}$$

It follows that Eq. (76) will reduce to Eq. (78):

$$\frac{m_{ev}}{Z} = C(RePr)^n \tag{78}$$

Taking logarithms on both sides Eq. (78) is written as shown in Eq. (79).

$$\ln\left[\frac{m_{ev}}{Z}\right] = \ln C + n \ln(RePr) \tag{79}$$

This is in the form of a linear equation as expressed in Eq. (80).

$$y = mx + c \tag{80}$$

The parts of Eq. (80) are represented as follows:

$$y = \ln\left[\frac{m_{ev}}{Z}\right], m = n, x = \ln(RePr), c = \ln C, \text{and } C = e^c$$

The following polynomial expressions shown in Eqs. (81)–(85) have been used according to Anwar and Tiwari [29] to determine density (ρ_v), viscosity (μ_v), specific heat (C_v) and thermal conductivity (k_v) of humid air. The physical properties of humid air were then used in computation of Reynolds number (Re) and Prandtl number (Pr).

$$\rho_v = \frac{353.44}{(T_i + 273.15)} \tag{81}$$

$$\mu_v = 1.718 \times 10^{-5} + \left(4.620 \times 10^{-8} T_i\right) \tag{82}$$

$$C_v = 999.2 + 0.1434 T_i + \left(1.101 \times 10^{-4} T_i^2\right) - \left(6.7581 \times 10^{-8} T_i^3\right) \tag{83}$$

$$k_v = 0.0244 + \left(0.6773 \times 10^{-4} T_i\right) \tag{84}$$

$$T_i = \frac{(T_b + T_v)}{2} \tag{85}$$

Measured data of black nightshade seeds temperature (T_b), exit humid air temperature (T_v), and exit humid air relative humidity (γ_v) were recorded. The weight of black nightshade seeds was precisely recorded during the drying period. Calculated data of moisture evaporated (m_{ev}) during drying, results of Eq. (77) representing (Z), Reynolds number (Re), and Prandtl number (Pr) were plotted. The values of y and x in Eq. (80) which correspond to Eq. (79) were evaluated for different time intervals and the constants C and n were obtained by linear regression analysis and used to evaluate the convective heat transfer coefficient of black nightshade seeds (h_b). The evaporative heat transfer coefficient (h_e) was then evaluated using Eq. (86) [28].

$$h_e = 16.273 \times 10^{-3} h_b \left(\frac{P(T_b) - \gamma_r P(T_r)}{T_b - T_r}\right) \tag{86}$$

From Jain and Tiwari [30], constant values of parameters used in modelling were adopted as follows: latent heat of vapourization (λ) as 2.26×10^6 J/kg, humid air velocity (v) as 0.01 m/s, and black nightshade seeds absorptivity (α_b) as 0.6.

2.11. Proposed simulation models for evaluation of temperature and moisture evaporated

The initial moisture content was determined according to Ref. [4] on AOAC method of analysis. 50 g of black nightshade seeds were placed in a moisture dish and both weights were taken. The seeds sample and moisture dish were placed in an oven and temperatures set at 105 °C. The samples were removed and placed in a desiccator. The final mass was obtained after cooling. A constant mass was measured and recorded. Moisture content (% db) at any given drying time t (hours) was obtained using Eq. (87).

$$M = \frac{m_i - m_t}{m_t} \times 100 \tag{87}$$

In Eq. (87), M is moisture content in (% db); m_i is initial mass of sample (g); and m_t is dried mass of sample (g) at time t (hours). The instantaneous drying rate of black nightshade seeds was computed using Eq. (88) where DR is the drying rate (g/g/h), Δm is change in mass (g), Δt is change in time (h), m_{i-1} is the sample mass (g) preceding a given instantaneous sample mass, m_i (g), t_{i-1} is the drying time (h) preceding a given instantaneous drying time, t_i (h), and m_d is the final mass (g) of dried sample.

$$DR = \frac{\Delta m}{\Delta t} = \frac{m_{i-1} - m_i}{m_d(t_{i-1} - t_i)} \tag{88}$$

The moisture ratio at different drying time was computed using Eq. (89) from the data for moisture content of black nightshade seeds. Equation (89) is based on the theory of thin layer drying and MR is moisture ratio; M_t is the moisture content (% db) at time t in hours; M_e is equilibrium moisture content (%), M_i is initial moisture content (% db).

$$MR = \frac{M_t - M_e}{M_i - M_e} \tag{89}$$

Greenhouse drying is complex and is under the influence of external variables in interaction with one another. The need for simple models to describe responses obtained from controlled black nightshade seeds drying experiments is therefore emphasized considering deterministic effects as given in Eqs.(90)–(92).

$$T_{b-pred} = f(t, \xi) \tag{90}$$

$$T_{r-pred} = f(t, \zeta) \tag{91}$$

$$m_{ev-pred} = f(t, \Omega) \tag{92}$$

In Eqs.(90)–(92), predicted black nightshade seeds temperature (T_b), greenhouse dryer room air temperature (T_r), and moisture evaporated

from black nightshade seeds (m_{ev}) are obtained as a result of a stimulus (predictor) known as drying time (t) according to a response function (f) based on a number of parameters which are indicated by the Greek letters (ξ), (ζ), and (Ω), respectively. Introducing stochastic effects of experimental error while considering the Gaussian probability density function (PDF) and cumulative distribution function (CDF), the relationship between predicted and experimental data is given in Eqs.(93)–(95).

$$T_{b-pred} \neq T_{b-expt} \tag{93}$$

$$T_{r-pred} \neq T_{r-expt} \tag{94}$$

$$m_{ev-pred} \neq m_{ev-expt} \tag{95}$$

Experimental data for (T_b), (T_r) and (m_{ev}) were collected for each drying time in solar, solar-exhaust gas, and exhaust gas modes of drying. Both experimental data and drying time were treated as stimuli for predicted data of (T_b), (T_r) and (m_{ev}). According to biological mechanism of black nightshade seeds drying process the response functions (f) were empirically selected as non-linear second order equations for predicting (T_b) and (T_r) following the Galilean process by posing the hypothesis in the form of mathematical models given in Eqs. (96) and (98). Moreover, for moisture evaporated from black nightshade seeds (m_{ev}), the response function (f) was selected as an exponential decay equation given in Eq. (98). Eqs.(96)–(98) have taken into account the interactions between one stimulus and the other.

$$T_{b-pred} = \xi_0 + \xi_1 t + \xi_2 T_{b-expt} + \xi_3 t T_{b-expt} + \xi_4 t^2 + \xi_5 \left(T_{b-expt}\right)^2 + \varpi \tag{96}$$

$$T_{r-pred} = \zeta_0 + \zeta_1 t + \zeta_2 T_{r-expt} + \zeta_3 t T_{b-expt} + \zeta_4 t^2 + \zeta_5 \left(T_{r-expt}\right)^2 + \varrho \tag{97}$$

$$m_{ev-pred} = \Omega_0 \left(1 - exp\left(-\Omega_1 (t)^{\Omega_2}\right)\right) + \Omega_3 \left(1 - exp\left(-\Omega_4 \left(m_{ev-expt}\right)^{\Omega_5}\right)\right) \tag{98}$$

Experimental data used in the modeling process of Eqs.(96)–(98) were divided into three data sets: training, validation, and testing. To fully specify the response functions (f), values of parameters (ξ), (ζ), and (Ω) were found through curve fitting in R statistical software.

3. Results and discussion

3.1. Fluid characteristics of solar-exhaust gas greenhouse dryer

The volume of exhaust gas ranged from 0.004 m^3 in connector one (CN1) to 1.5 m^3 in connector six and from 0.3 m^3 in tube one (TB1) to 1.8 m^3 in tube six. Similarly, exhaust gas mass ranged from 0.003 kg in CN1 to 1.1 kg in CN6 and from 0.2 kg in TB1 to 1.3 kg in TB6 as shown in Fig. 9. The average density of exhaust gas in the set up was 0.7218 kg/m^3. Mass of exhaust gas and volume increased from CN1 to CN6 and from TB1 to TB6 because the distance of connectors and tubes from exhaust manifold increased from 2.1 m in CN1 to 16.3 m in CN6 and from 4.6 m in TB1 to 18.8 m in TB6. Increased length of the hybrid recuperative heat exchanger (HRHE) improved residence time and led to high heat energy transfer from exhaust gas.

The time taken for exhaust gas to fill connectors and tubes decreased with increased volumetric flow rate as shown in Fig. 10. Volumetric flow rates ranged from 0.0042 to 0.0167 m^3/s and the rates increased with increasing engine speed which ranged from 750 to 2500 rpm. At the lowest engine speed of 750 rpm, it took exhaust gas 418 s to reach the furthest tube (TB6) while at the highest engine speed of 2500 rpm 105 s elapsed before exhaust gas could reach TB6. The temperature of exhaust gas at 750 rpm engine speed was 197.19 °C and it increased gradually with increased engine speed to 359.82 °C at 2000 rpm. There was a slight decrease in exhaust gas temperature at 2250 rpm to 356.98 °C and a further decrease to 357.36 °C. However, statistically, the results of a single factor analysis of variance (ANOVA) indicated no significant difference in the temperatures of exhaust gas for the range of engine speeds between 1750 and 2500 rpm, (F_{calc} = 1.3289, $F_{crit,0.95}$ = 2.9011, $F_{crit,0.99}$ = 4.4594 and p-value = 0.2822). In previous study, thermal conductivity was found to be increasing with temperature showing maximum enhancement of 16.8 % for 1 % volume fraction and 65 °C temperature, nevertheless, viscosity showed decrement with temperature rise with maximum drop of 30.7 % for the similar working condition [31].

The mas flow rate of exhaust gas ranged from 11.32 to 45.07 kg/h as shown in Fig. 11. Higher engine speeds of 2000 to 2500r rpm resulted in higher mass flow rates of 41.46–45.07 kg/h. The available energy in exhaust gas at the lowest mass flow rate of 11.32 kg/h was 2082.32 kJ/h. At 1000 rpm the available energy was 2591.28 kJ/h. Increasing the engine speed by a step value of 250 rpm resulted in increased available energy ranging from 6795.84 to 16002.56 kJ/h. Moreover, this corresponded to engine speeds of 1250–2500 rpm. The Nusselt number of exhaust gas flow in all tubes was 3.66 because the flow was laminar in all from TB1 to TB6. The Reynolds number of exhaust gas in tubes increased with increased velocity as shown in Fig. 11. Velocity of exhaust gas in flow in tubes ranged from 0.035 to 0.14 m/s. Clearly, these low velocities affected the time taken for exhaust gas to fill the tubes. Experimental analysis of variance assuming that tube location had no effect on exhaust gas residence time resulted in: F_{calc} = 6.516, $F_{crit,0.95}$ = 2.249, $F_{crit,0.99}$ = 3.124, and p-value = 3.75×10^{-5}. Thus, exhaust gas residence times for all the engine speeds ranging from 750 to 2500 rpm were significantly different from each other at both 95 and 99 % confidence interval. A two factor ANOVA without replication considering the effects of tube location resulted in: $F_{calc.ES}$ = 21.1184, $F_{crit.ES,0.95}$ = 2.2852, $F_{crit.ES,0.99}$ = 3.20, and p-value = 8.08×10^{-11}; $F_{calc.TB}$ = 18.9296,

Fig. 9. Exhaust gas volume and mass.

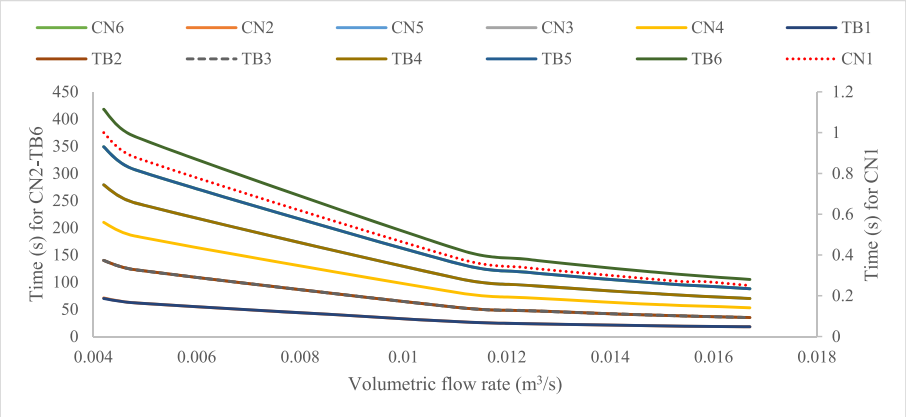

Fig. 10. Time taken for exhaust gas to fill connectors and tubes.

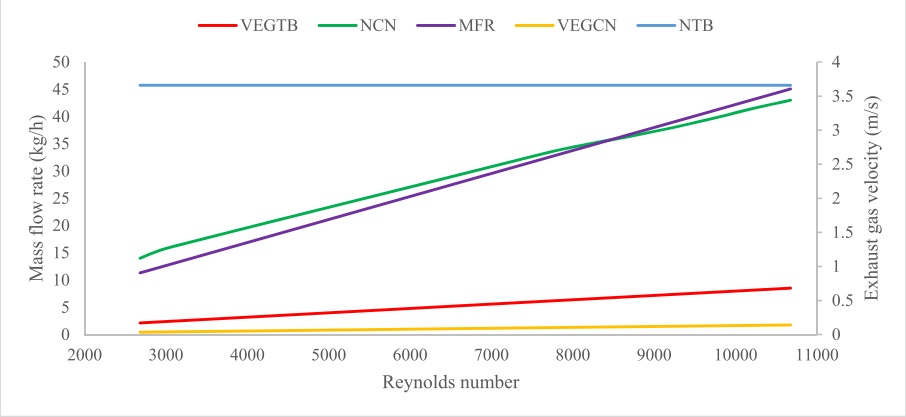

Fig. 11. Exhaust gas fluid properties in hybrid recuperative heat exchanger.

$F_{crit.TB,0.95} = 2.4851$, $F_{crit.TB,0.99} = 3.5919$, and p-value $= 4.38 \times 10^{-9}$. Therefore, exhaust gas residence times in the tubes were significantly different from each other and it is concluded with 95 and 99 % confidence that blocking against the effects of tube location for the experimental analysis is essential.

Further analysis to determine Fisher's least significant difference (LSD) was determined and 245 s was found at 95 % confidence interval as shown in Table 1. Therefore, at 750 rpm exhaust gas residence time of 279 s in TB4 was significantly different from the following times in seconds i.e., 27, 24, 21, 19, 19, and 18 recorded in TB1 from 1250 to 2500 rpm engine speed in a step value of 250 rpm. Applying the same argument in TB1, 349, 368 and 418 s was significantly different from all the residence times recorded in the tube at volumetric flow rate range of 0.0042–0.0167 m^3/s. In addition, 349 s was different from the times recorded in TB2 and TB3 from 0.0111 to 0.0167 m^3/s, while in TB4, it ranged from 0.0123 to 0.0167 m^3/s. In TB5 residence times recorded to correspond with volumetric flow rates from 0.0154 to 0.0167 m^3/s were significantly different from 349 s. Similarly, 418 s recorded in TB6 at 750 rpm was significantly different from all the residence time in TB2 ranging from 140 to 35 s and corresponding to volumetric flow rates of 0.0042–0.0167 m^3/s. However, in TB3, TB4, TB5 and TB6 418 s was significantly different from all the times recorded in the volumetric flow rate range of 0.0111–0.0167 m^3/s. The abbreviated legends in Fig. 11 are: velocity of exhaust gas in tubes (VEGTB), Nusselt number in connectors (NCN), mass flow rate of exhaust gas (MFR), velocity of exhaust gas in connectors (VEGCN) and Nusselt number in tubes (NTB).

Fisher's least significant difference determined at 99 % confidence interval was 363 s as shown in Table 2. Taking that into consideration, 418 s recorded at 750 rpm in TB6 was significantly different from all the exhaust gas residence times recorded at less than 55 s. Fig. 11 shows a plot of fluid properties of exhaust gas with velocity in connectors higher than those in tubes. The dimensionless Nusselt number in connectors increased in tandem with exhaust gas mass flow rate but remained

Table 1
Residence time difference at 95 % confidence interval for LSD = 245 s.

Volumetric flow rate (m^3/s)	Tube location	Residence time difference (s)	Absolute value
0.0042	TB1	|349 – 70|	279
0.0048	TB2	|418 – 123|	295
0.0111	TB3	|349 – 80|	269
0.0123	TB4	|349 – 95|	254
0.0140	TB5	|418 – 105|	313
0.0154	TB6	|418 – 114|	304
0.0158	TB1	|279 – 19|	260
0.0167	TB2	|349 – 35|	314

Table 2
Residence time difference at 99 % confidence interval for LSD = 363 s.

Volumetric flow rate (m^3/s)	Tube location	Residence time difference (s)	Absolute value
0.0042	TB1	|418 – 70|	348
0.0111	TB3	|418 – 53|	365
0.0123	TB1	|418 – 24|	394
0.0140	TB1	|418 – 21|	397
0.0154	TB1	|418 – 19|	399
0.0158	TB1	|418 – 19|	399
0.0167	TB3	|418 – 53|	365

relatively constant in tubes. High temperatures of exhaust gas were associated with high mass flow rates, but temperature gradient inversely influenced heat energy transfer rate between gaseous streams. Convection current in the drying environment caused hotter and lighter air to move up as colder and heavier air moved down.

The results of major head losses due to friction in connectors and tubes of the HRHE are shown in Table 3 and Table 4 respectively. The plots of frictional head losses and friction factors and their variation with Reynolds number in connectors and tubes are shown in Figs. 12 and 13. In Fig. 12, the values of frictional head loss are higher as compared to the friction factor as applied in connectors of the heat exchanger. For this reason, frictional head loss was plotted on the primary vertical axis and the friction factor was plotted on the secondary vertical axis. The two plots were made with Reynolds number on the primary horizontal axis. It can be observed that for all the connectors, the frictional head loss increased with increasing Reynolds number. This observation is equally true for the tubes as plotted in Fig. 13. In addition, the frictional head loss increased from CN1 to CN6, with connector number six posting the highest value of 71 m. The high head loss is attributed to variation of longitudinal distance from exhaust manifold from which it can be shown that CN6 was 16.3 m away. The friction factor graph in Fig. 12 shows that Reynolds' number increased as the friction factor decreased. This is explained by higher velocities of exhaust gas in connectors of the HRHE. In Fig. 13, the values of frictional head loss in tubes were lower in comparison to the friction factor. It was necessary that friction factor should be plotted on the primary vertical axis as frictional head loss took the secondary vertical axis so that Reynolds number values were plotted on the primary horizontal axis. The graph of friction factor shows a decreasing trend in Fig. 13, with increased Reynolds number which in turn increase with increased velocities as the engine speed is increased.

3.2. Thermal characteristics of solar-exhaust gas greenhouse dryer

Experimental and model predicted temperature profiles for greenhouse dryer operated on solar mode (SM), solar-exhaust gas mode (SEGM) and exhaust gas mode (EGM) of drying are shown in Fig. 14. Solar mode of drying was carried out between 6:00 a.m. and 5:00 p.m.; solar-exhaust gas mode was performed between 6:00 a.m. and 4:00 a.m.; and lastly exhaust gas mode of drying was performed between 5:00 p.m. and 7:00 a.m. on different dates. In solar mode, greenhouse dryer room air temperature peaked at 58.46 °C at 2:00 p.m. then decreased to a low value of 29.05 °C at 5:00 p.m. The time between 12 noon and 2:00 p.m. was characterized by high solar energy intensity which accounted for high temperatures. Moreover, the day had a clear sky and cloud cover effects were not experienced. In solar-exhaust gas mode temperature peaked at 61.97 °C at 12 noon then slightly dropped to 56.34 °C at 4:00 p.m. In this mode, supplemental heat energy from exhaust gas was supplied to keep the temperatures high because the day was characterized by low solar radiation and high cloud cover in the sky. In exhaust gas mode, the average temperature for the entire drying time was 28.85 °C with a minimum of 25.75 °C and a maximum of 30.77 °C. Exhaust gas heat energy was continuously supplied for the period because it was nighttime, and no solar radiation was expected. The abbreviated legends in Fig. 14 are: experimental greenhouse dryer temperature in solar mode (ExGHDT-SM), predicted greenhouse dryer temperature in solar mode (PrGHDT-SM), experimental greenhouse dryer temperature in solar-exhaust gas mode (ExGHDT-SEGM), predicted greenhouse dryer temperature in solar-exhaust gas mode (PrGHDT-SEGM), experimental greenhouse dryer temperature in exhaust gas mode (ExGHDT-EGM) and predicted greenhouse dryer temperature in exhaust gas mode (PrGHDT-EGM).

Table 3
Major head losses in connectors.

Re_{CN}	f_{CN}	Frictional head loss in connectors (m)					
		CN1	CN2	CN3	CN4	CN5	CN6
2681	0.1860	0.7	1.6	2.5	3.5	4.4	5.3
3048	0.1637	0.9	2.0	3.2	4.3	5.5	6.6
7055	0.0707	4.3	10	16	21	27	33
7865	0.0635	5.3	12	19	27	34	41
8917	0.0560	6.7	16	25	34	42	51
9819	0.0508	8.1	19	30	40	51	62
10073	0.0496	8.4	20	31	42	53	65
10674	0.0468	9.3	22	34	46	59	71

As a result of changes in temperature, moisture evaporated in the three modes of drying were plotted in Fig. 15. In all the drying modes, the first 4 h of drying resulted in high moisture evaporation because of fast drying rates as illustrated by the negative gradient parts of the curves. The drying rates were computed as ranging from 5.1106 to 0.0713 g/g/h for SM, 1.6626–0.0607 g/g/h for SEGM and 16.181–0.0942 g/g/h for EGM. High moisture evaporation is attributed to gradual increase in temperature as heat energy is supplied but the drying rate is dependent upon several factors such as initial moisture content of product, sample mass (g) preceding a given instantaneous sample mass, drying time (h) preceding a given instantaneous drying time, and final mass (g) of dried product sample. During these periods relative humidity dropped from 88 to 27 % in SM and from 39 to 15 % in SEGM. However, in EGM relative humidity increased from 52 to 84 % because water vapour from the open cooling system of the engine in use affected the dryer's performance. For all the drying modes, it can be observed from Fig. 15 that the rate of moisture evaporation asymptotically gets to zero value. The abbreviated legends in Fig. 15 are: experimental moisture evaporated in solar mode (ExME-SM), predicted moisture evaporated in solar mode (PrME-SM), experimental moisture evaporated in solar-exhaust gas mode (ExME-SEGM), predicted moisture evaporated in solar-exhaust gas mode (PrME-SEGM), experimental moisture evaporated in exhaust gas mode (ExME-EGM) and predicted moisture evaporated in exhaust gas mode (PrME-EGM).

Kinetic energy is a function of exhaust gas volumetric flow rate which in turn is a function of engine speed. High engine speeds lead to high exhaust gas flow rates. Plotting exhaust gas velocity against kinetic energy results in Figs. 16 and 17. From the graphs, kinetic energy of exhaust gas in tubes were generally lower as compared to that in connectors because exhaust gas velocities were higher in connectors as compared to those of tubes. Kinetic energy increased with increased velocity for both tubes and connectors to a maximum of 39.79 kJ/h in connectors and 1.289×10^{-2} kJ/h in tubes. A single factor ANOVA performed with the assumption that connectors' location had no significant effect on kinetic energy showed that: $F_{calc} = 3.171$, $F_{crit,0.95} = 2.249$, $F_{crit,0.99} = 3.124$, and p-value $= 9.17 \times 10^{-3}$. Therefore, at $\alpha = 0.05$ and 0.01 it is concluded with 95 and 99 % confidence that blocking against the effects of connector location is necessary.

Performing a two-factor ANOVA without replication and considering the effects of connectors location resulted in: $F_{calc.VEG} = 10.8359$, $F_{crit.VEG,0.95} = 2.2852$, $F_{crit.VEG,0.99} = 3.20$, and p-value $= 3.49 \times 10^{-7}$; $F_{calc.CN} = 20.3339$, $F_{crit.CN,0.95} = 2.4851$, $F_{crit.CN,0.99} = 3.5919$, and p-value $= 1.79 \times 10^{-9}$. From statistical results, therefore, kinetic energy in connectors were significantly different from each other and further analysis to determine Fisher's least significant difference was performed. Considering the null hypothesis (H_0) that there is no difference in the kinetic energy recorded in the six connectors and the alternative hypothesis (H_a) that at least one of the values of kinetic energy differ from the others, at $\alpha = 0.05$ any two values whose difference was equal to or greater than LSD = 23.85 kJ/h were regarded significantly different. However, at $\alpha = 0.01$ and applying the same criteria LSD was found and used as 35.29 kJ/h. A summary of the differences are given in Table 5 and Table 6. Previous studies on exhaust gases energy recoverable from compression ignition engine using diesel and biodiesel have reported the maximum recovered energy from the exhaust as 60 % of the brake power when an engine was operated on diesel [32]. When the engine used biodiesel the maximum recovered energy from the exhaust

Table 4
Major head losses in tubes.

Re_{TB}	f_{TB}	Frictional head loss in tubes (m)					
		TB1	TB2	TB3	TB4	TB5	TB6
344	0.0700	0.00014	0.00022	0.00031	0.00039	0.00048	0.00056
391	0.0675	0.00016	0.00025	0.00035	0.00045	0.00054	0.00064
905	0.0625	0.00036	0.00059	0.00081	0.00104	0.00126	0.00148
1008	0.0620	0.00040	0.00065	0.00090	0.00116	0.00141	0.00166
1143	0.0610	0.00046	0.00074	0.00103	0.00131	0.00159	0.00188
1259	0.0605	0.00050	0.00082	0.00113	0.00144	0.00175	0.00207
1291	0.0600	0.00052	0.00084	0.00116	0.00148	0.00180	0.00212
1368	0.0590	0.00055	0.00089	0.00123	0.00157	0.00191	0.00225

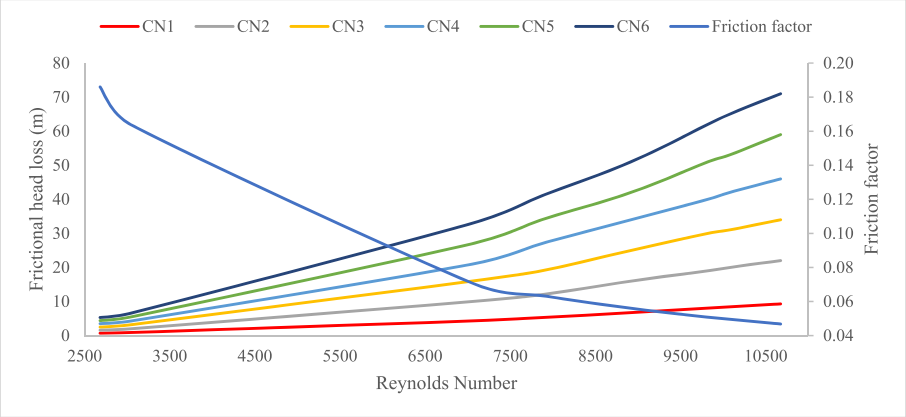

Fig. 12. Frictional head loss and friction factor in connectors.

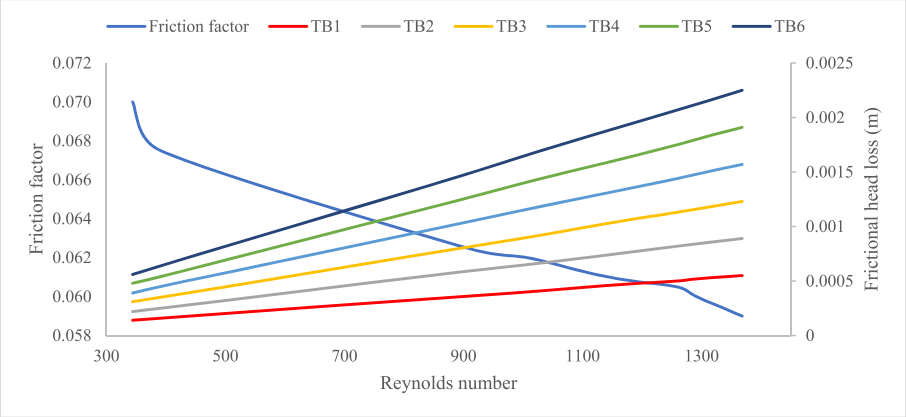

Fig. 13. Friction factor and frictional head loss in tubes.

was 78 % of the brake power. The maximum recovered energy from the exhaust was 29.1 % lower when the engine was fueled on diesel than when biodiesel was used at 1000 rpm and 18 Nm. The recovered energy from the exhaust gases increased with increased engine speed and load to an optimum. Energy recovered from the exhaust gases when the engine was operated on biodiesel was more than when the engine used diesel. However, with better and improved energy recovery systems more energy could be recovered.

4. Conclusions

The current study aimed to experimentally validate fluid and thermal characteristics of a solar-exhaust gas greenhouse dryer and the following conclusions were drawn from the study.

- Available energy in exhaust gas was found in the range of 2082.32–16002.5 kJ/h, corresponding to temperatures of 197.19–359.82 °C as a result of engine speeds varied from 750 to 2500 rpm.
- Fluid and thermal characteristics of the dryer were reported for three modes of drying: solar mode (SM), solar-exhaust gas mode (SEGM), and exhaust gas mode (EGM). Consequently, the dryer room air temperature were found as: 14.82–58.46 °C, 34.49–61.97 °C and 25.75–30.77 °C respectively. Moisture evaporated as a result of temperature variations were computed as: 0–20.8 g, 0–17.79 g and 0–22.33 g respectively.
- Kinetic energy in exhaust gas increased with increased velocity for both tubes and connectors to a maximum of 39.79 kJ/h in connectors and 1.289×10^{-2} kJ/h in tubes. Reynolds number ranged from 2681

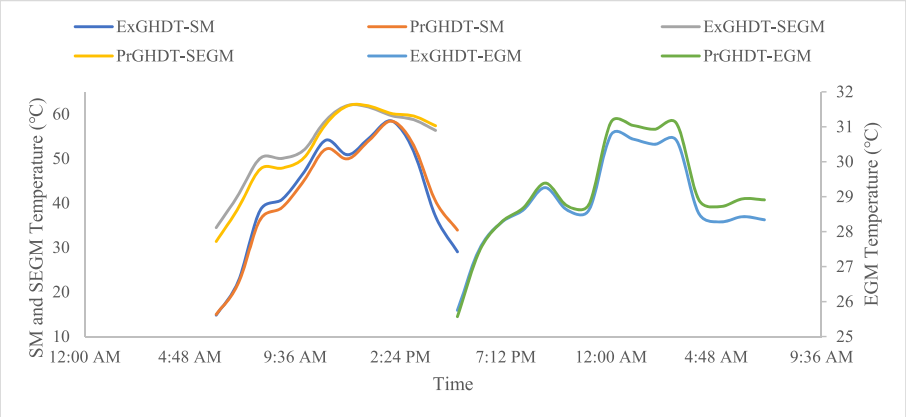

Fig. 14. Greenhouse dryer room air temperature profile.

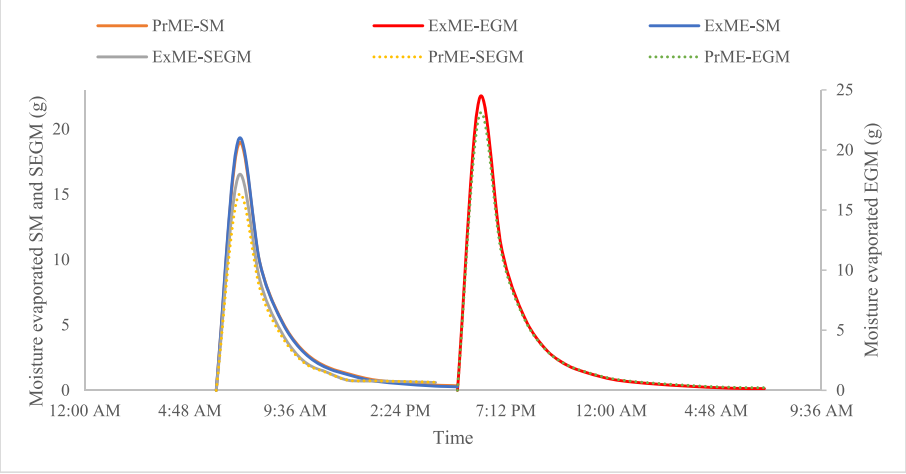

Fig. 15. Moisture evaporated in three modes of drying.

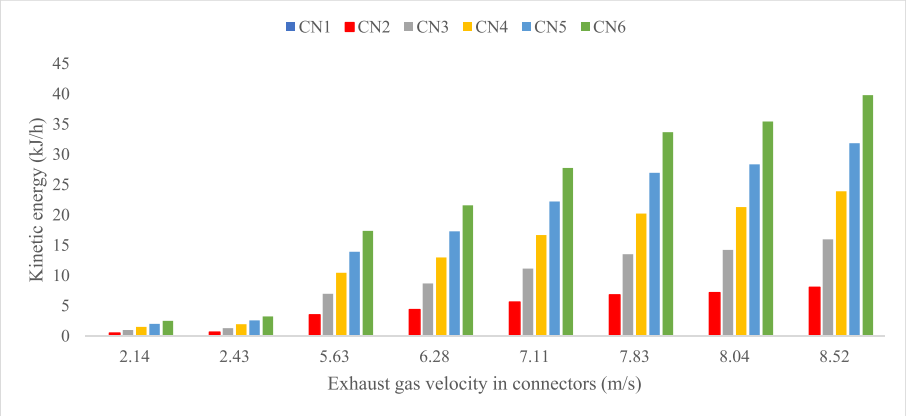

Fig. 16. Kinetic energy in exhaust gas flowing through connectors.

to 10674 in connectors and 344–1368 in tubes, Nusselt number ranged from 14 to 43 in connectors and constant at 3.66 in tubes.

- Fluid characteristics of exhaust gas included: average density of 0.7218 kg/m^3, volumetric flow rates from $4.2 \times 10^{-3} - 1.67 \times 10^{-2}$ m^3/s, maximum residence time of 418 s in HRHE, mass flow rates from 11.32 to 45.07 kg/h, velocity in connectors ranging from 2.14 to 8.52 m/s, and velocity in tubes from 0.035 to 0.14 m/s.
- The drying rates were computed as ranging from 5.1106 to 0.0713 g/g/h for SM, 1.6626–0.0607 g/g/h for SEGM and 16.181–0.0942 g/g/h for EGM. Relative humidity dropped from 88 to 27 % in SM and from 39 to 15 % in SEGM. However, in EGM relative humidity increased from 52 to 84 % because water vapour from the open cooling system of the engine in use affected the dryer's performance.

This study was limited to harvesting of exhaust gas energy from a

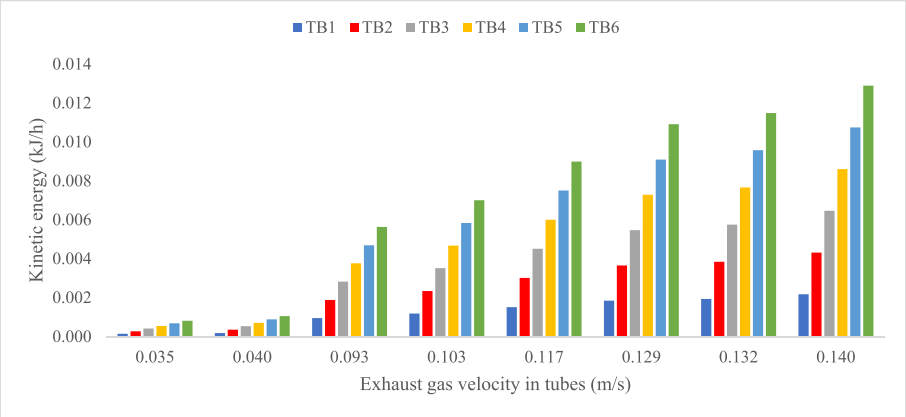

Fig. 17. Kinetic energy in exhaust gas flowing through tubes.

Table 5
Kinetic energy difference at 95 % confidence interval for LSD = 23.85 kJ/h.

Velocity (m/s)	Connector location	Kinetic energy difference (kJ/h)	Absolute value
2.14	CN1	|27.77 – 0.007|	27.763
2.43	CN2	|27.77 – 0.660|	27.110
5.63	CN3	|33.67 – 6.980|	26.690
6.28	CN4	|39.79 – 12.99|	26.800
7.11	CN6	|0.007 – 27.77|	27.763
7.83	CN6	|0.007 – 33.67|	33.663
8.04	CN1	|27.77 – 0.101|	27.669
8.52	CN2	|33.67 – 8.050|	25.620

Table 6
Kinetic energy difference at 99 % confidence interval for LSD = 35.29 kJ/h.

Velocity (m/s)	Connector location	Kinetic energy difference (kJ/h)	Absolute value
2.14	CN4	|39.79 – 1.510|	38.280
2.43	CN3	|39.79 – 1.300|	38.490
5.63	CN2	|39.79 – 3.520|	36.270
6.28	CN2	|39.79 – 4.370|	35.420
7.11	CN1	|35.43 – 0.079|	35.351
7.83	CN1	|35.43 – 0.096|	35.334
8.04	CN1	|35.43 – 0.101|	35.329
8.52	CN1	|35.43 – 0.114|	35.316

diesel engine and utilizing the energy to dry black nightshade seeds in a solar-exhaust gas greenhouse dryer. The scope for future research would include: focusing on determination of tempering period for black nightshade seeds to advance understanding; finding an equation that best describes sorption data of black nightshade seeds; use of exhaust gas energy generated from spark ignition engines in farms; exploring a method to store the continuously produced heat energy from exhaust gas and diesel engine's cooling system; finding solutions capable of reversing or controlling the phenomenon of exhaust gas particles adhering to the wall of the heat exchanger, as this may increase thermal resistance over a prolonged period of time; conducting studies on moisture sorption isotherms of black nightshade seeds for equilibrium moisture content evaluation; and determining the effect of volumetric shrinkage, moisture diffusivity and geometric changes on heat and mass transfer in black nightshade seeds drying.

CRediT authorship contribution statement

George Onyango Orido: Writing – review & editing, Writing – original draft, Visualization, Validation, Methodology, Investigation, Formal analysis, Data curation, Conceptualization. **Erick Kiplangat Ronoh:** Writing – review & editing, Supervision, Project administration. **Patrick Ochuodho Ajwang:** Writing – review & editing, Supervision, Project administration. **Benson Baari Gathitu:** Writing – review & editing, Supervision, Project administration.

Declaration of competing interest

The authors declare that they have no known competing financial interests or personal relationships that could have appeared to influence the work reported in this paper.

Data availability

Data will be made available on request.

Acknowledgments

The authors would like to appreciate GeoPrice eligibility and Research4Life programs for the article publishing charge waiver and discount which allows this paper to be in a gold open access journal. The valuable time and service of the editorial team in improving this article is appreciated. A manuscript of this kind is inevitably a team operation, and gratitude is due particularly to reviewers.

References

[1] G.O. Orido, E.K. Ronoh, P.O. Ajwang, B.B. Gathitu, Performance assessment of hybrid recuperative heat exchanger for diesel engine generated exhaust gas, International Journal of Thermofluids 100392 (2023), https://doi.org/10.1016/j.ijft.2023.100392.
[2] D. Jain, G.N. Tiwari, Effect of greenhouse on crop drying under natural and forced convection II. Thermal modelling and experimental validation, Energy Convers. Manag. 45 (17) (2004) 2777–2793, https://doi.org/10.1016/j.enconman.2003.12.011.
[3] M.I. Alam, M.M. Nuhash, A. Zihad, T.H. Nakib, M.M. Ehsan, Conventional and emerging CSP technologies and Design Modifications: research Status and recent Advancements, International Journal of Thermofluids 100406 (2023), https://doi.org/10.1016/j.ijft.2023.100406.
[4] G.O. Orido, E.K. Ronoh, P.O. Ajwang, B.B. Gathitu, Evaluation of thin layer models for simulating drying kinetics of black nightshade seeds in a solar-exhaust gas greenhouse dryer, Bioprocess Eng. 7 (1) (2023) 10–31, https://doi.org/10.11648/j.be.20230701.12.
[5] P.S. Chauhan, A. Kumar, C. Nuntadusit, J. Banout, Thermal modeling and drying kinetics of bitter gourd flakes drying in modified greenhouse dryer, Renew. Energy 118 (2018) 799–813, https://doi.org/10.1016/j.renene.2017.11.069.
[6] I. Harris, A.J. Rivas, M.D.L.A.O. Del, M.Z. Saghir, Recent developments in phase change material-based solar water heating systems: Insights on research trends and opportunities, International Journal of Thermofluids 20 (2023) 100359, https://doi.org/10.1016/j.ijft.2023.100359.
[7] S.M. Al-Weheibi, M.M. Rahman, M.Z. Saghir, Three-dimensional non-Darcy free convective heat transfer flow in a bidisperse porous medium within a cubical cavity, International Journal of Thermofluids 20 (2023) 100413, https://doi.org/10.1016/j.ijft.2023.100413.

[8] G.O. Orido, G.M. Ngunjiri, M.R. Njue, Exhaust gases energy recovered from internal combustion engine for useful applications, Journal of Mechanical and Civil Engineering 14 (3) (2017) 1–7, https://doi.org/10.9790/1684-1403070107.
[9] P.S. Chauhan, A. Kumar, Thermal modeling and drying kinetics of gooseberry drying inside north wall insulated greenhouse dryer, Appl. Therm. Eng. 130 (2018) 587–597, https://doi.org/10.1016/j.applthermaleng.2017.11.028.
[10] S.M. Ibrahim, A. Abdelmaksoud, W. Helal, Heat transfer characteristics for multi-silicon ingots irradiation in a typical research reactor, International Journal of Thermofluids 20 (2023) 100411, https://doi.org/10.1016/j.ijft.2023.100411.
[11] A. Nassar, E. Nassar, I. Rivilla, J. Labidi, A.G. Fernández, F. Sarasini, M. Younis, Enhancing the thermal transfer properties of phase change material for thermal energy storage by impregnating hybrid nanoparticles within copper foams, Results in Engineering 21 (2024) 101885, https://doi.org/10.1016/j.rineng.2024.101885.
[12] S.T.P. Purayil, S.A.B. Al-Omari, E. Elnajjar, Effect of Hydrogen Blending on the combustion performance, Emission, and cycle-to-cycle variation characteristics of a single-Cylinder GDI spark ignition Dual-fuel engine, International Journal of Thermofluids 100403 (2023), https://doi.org/10.1016/j.ijft.2023.100403.
[13] G.O. Orido, M.R. Njue, G.M. Ngunjiri, Grain drying simulation in a GT-380 dryer using energy recovered from ICE exhaust, Journal of Agriculture and Veterinary Science 10 (6) (2017) 1–6, https://doi.org/10.9790/2380-1006020106.
[14] P.S. Chauhan, A. Kumar, B. Gupta, A review on thermal models for greenhouse dryers, Renew. Sustain. Energy Rev. 75 (2017) 548–558, https://doi.org/10.1016/j.rser.2016.11.023.
[15] G.O. Orido, G.M. Ngunjiri, M.R. Njue, Comparison of thermal energy lost through exhaust gases at various engine speeds and Torque loads for diesel and biodiesel fuels, Journal of Mechanical and Civil Engineering 14 (3) (2017) 8–12, https://doi.org/10.9790/1684-1403070812.
[16] Z. Al Hajaj, M.Z. Saghir, Numerical study on the influence of embedded PCM tubes on the energy storage properties of the geothermal energy pile, International Journal of Thermofluids 20 (2023) 100416, https://doi.org/10.1016/j.ijft.2023.100416.
[17] B. Sun, L. Tian, J. Hou, Q. An, Multi-criteria assessment and optimization of a natural gas-fed solid oxide fuel cell combined heat and power system, International Journal of Thermofluids 20 (2023) 100420, https://doi.org/10.1016/j.ijft.2023.100420.
[18] G.O. Orido, E.K. Ronoh, P.O. Ajwang, B.B. Gathitu, Influence of solar-exhaust gas greenhouse drying modes on Viability of black nightshade seeds, Journal of Chemical, Environmental and Biological Engineering 7 (2) (2023) 44–56, https://doi.org/10.11648/j.jcebe.20230702.11.
[19] H. Ehsani, F.N. Roudbari, S.S. Namaghi, D.D. Ganji, Investigating thermal performance enhancement in perforated pin fin arrays for cooling electronic systems through integrated CFD and deep learning analysis, Results in Engineering (2024) 102016, https://doi.org/10.1016/j.rineng.2024.102016.
[20] F. Alnaimat, A. Rahhal, B. Mathew, Thermal and hydraulic performance investigation of microchannel heat sink with sidewall square pin-fins, Results in Engineering 101896 (2024), https://doi.org/10.1016/j.rineng.2024.101896.
[21] R. Bardera, Á.A. Rodríguez-Sevillano, E. Barroso, J.C. Matías, A.L.C. Alcaraz, Numerical analysis of the thermal convection through a flat plate in Martian conditions, Results in Engineering 102029 (2024), https://doi.org/10.1016/j.rineng.2024.102029.
[22] Z.M. Omara, W.H. Alawee, A. Basem, A.D.J. Al-Bayati, Heat loss reduction techniques for walls in solar stills: a review, Results in Engineering 101996 (2024), https://doi.org/10.1016/j.rineng.2024.101996.
[23] P.S. Chauhan, A. Kumar, C. Nuntadusit, Thermo-environomical and drying kinetics of bitter gourd flakes drying under north wall insulated greenhouse dryer, Sol. Energy 162 (2018) 205–216, https://doi.org/10.1016/j.solener.2018.01.023.
[24] A. Kumar, G.N. Tiwari, Thermal modelling of a natural convection greenhouse drying system for jaggery: an experimental validation, Sol. Energy 80 (9) (2006) 1135–1144, https://doi.org/10.1016/j.solener.2005.09.011.
[25] T.K. Nguyen, M. Mondor, C. Ratti, Shrinkage of cellular food during air drying, J. Food Eng. 230 (2018) 8–17, https://doi.org/10.1016/j.jfoodeng.2018.02.017.
[26] C. Ratti, Shrinkage during drying of foodstuffs, J. Food Eng. 23 (1) (1994) 91–105, https://doi.org/10.1016/0260-8774(94)90125-2.
[27] D. Jain, G.N. Tiwari, Effect of greenhouse on crop drying under natural and forced convection I: evaluation of convective mass transfer coefficient, Energy Convers. Manag. 45 (5) (2004) 765–783, https://doi.org/10.1016/S0196-8904(03)00178-X.
[28] G.N. Tiwari, S. Kumar, O. Prakash, Evaluation of convective mass transfer coefficient during drying of jaggery, J. Food Eng. 63 (2) (2004) 219–227, https://doi.org/10.1016/j.jfoodeng.2003.07.003.
[29] S.I. Anwar, G.N. Tiwari, Convective heat transfer coefficient of crops in forced convection drying—an experimental study, Energy Convers. Manag. 42 (14) (2001) 1687–1698, https://doi.org/10.1016/S0196-8904(00)00160-6.
[30] D. Jain, G.N. Tiwari, Effect of greenhouse on crop drying under natural and forced convection II. Thermal modelling and experimental validation, Energy Convers. Manag. 45 (17) (2004) 2777–2793, https://doi.org/10.1016/j.enconman.2003.12.011.
[31] B. Mehta, D. Subhedar, H. Panchal, K.K. Sadasivuni, Stability and thermophysical properties enhancement of Al2O3-water nanofluid using cationic CTAB surfactant, International Journal of Thermofluids 20 (2023) 100410, https://doi.org/10.1016/j.ijft.2023.100410.
[32] G.O. Orido, *Exhaust gases Energy Recoverable from Compression Ignition Engine Using Diesel and Biodiesel* (Master's Dissertation, EGERTON UNIVERSITY, 2018. http://41.89.96.81:8080/xmlui/handle/123456789/1480.